Anomalies in the electronic structure of a 5*d* transition metal oxide, IrO_2

Swapnil Patil,[1,2] Aniket Maiti,[1] Surajit Dutta,[1] Khadiza Ali,[1] Pramita Mishra,[1] Ram Prakash Pandeya,[1] Arindam Pramanik,[1] Sawani Datta,[1] Srinivas C. Kandukuri,[1] and Kalobaran Maiti[1,*]

[1]*Department of Condensed Matter Physics and Materials Science, Tata Institute of Fundamental Research, Homi Bhabha Road, Colaba, Mumbai-400005, India*

[2]*Department of Physics, Indian Institute of Technology (Banaras Hindu University), Varanasi-221005, India*

(Received 14 June 2021; accepted 22 October 2021; published 2 November 2021)

Ir-based materials have drawn much attention due to the observation of insulating phase believed to be driven by spin-orbit coupling, while Ir 5*d* states are expected to be weakly correlated due to their large orbital extensions. IrO_2, a simple binary material, shows a metallic ground state which seems to deviate from the behavior of most other Ir-based materials and varied predictions in this material class. We studied the electronic structure of IrO_2 at different temperatures, employing high-resolution photoemission spectroscopy with photon energies spanning from ultraviolet to hard *x*-ray range. Experimental spectra exhibit a signature of enhancement of Ir-O covalency in the bulk compared to the surface electronic structure. The branching ratio of the spin-orbit split Ir core-level peaks is found to be larger than its atomic values and it enhances further in the bulk electronic structure. Such deviation from the atomic description of the core-level spectroscopy manifests the enhancement of the orbital moment due to the uncompensated electric field around Ir sites. The valence-band spectra could be captured well within the density functional theory. The photon energy dependence of the features in the valence-band spectra and their comparison with the calculated results show dominant Ir 5*d* character of the features near the Fermi level; O 2*p* peaks appear at higher binding energies. Interestingly, the O 2*p* contributions of the feature at the Fermi level are significant, and it enhances at low temperatures. This reveals an orbital selective enhancement of the covalency with cooling, which is an evidence against the purely spin-orbit coupling based scenario proposed for these systems.

DOI: 10.1103/PhysRevMaterials.5.115001

I. INTRODUCTION

Transition metal oxides have been drawing much attention during the past few decades due to their exotic properties arising primarily from the interplay of electron correlation (U), covalency, spin-orbit coupling (SOC), and coupling with various collective degrees of freedom [1,2]. With the increase in radial extension of the *d* orbitals, the correlation strength among them is expected to reduce and subsequently, the other degrees of freedom become more dominant. In that respect, 4*d* oxides also show plethora of interesting properties [3]. Materials in the 5*d* family provide additional interest due to the strong SOC. For example, Ir-based compounds are fascinating due to a variety of physical properties exhibited by them, like Mott insulators [4], signature of density waves in the insulating phase [5], topological insulators [6–8], Weyl semimetals and axion insulators [9], etc. Heterostructures involving 4*d* and 5*d* oxides show exotic properties at the interface [10]. Such varied behavior is ascribed to the peculiar nature of the 5*d* electrons, which are believed to lie at the border between the highly correlated Mott state of 3*d* transition metal electrons and the itinerant behavior exhibited by the mobile *sp* conduction electrons. Various competing interactions such as crystalline electric field (CEF) splitting, SOC, and U compete with each other, giving rise to diverse exotic properties. To understand the behavior of the Ir 5*d* electrons, it is important to study them under reduced crystalline complexity. Since the aforementioned interactions are dominated by the on-site interactions (local), it is expected that such a study will manifest the intended behavior of Ir 5*d* electrons. IrO_2 is one such simple binary compound and offers a good platform for such investigations. While IrO_2 has been drawing attention for a long time [11–13], there is a recent revival of interest in the study of the properties of this compound, emphasizing the importance of spin-orbit coupling in this material [14–16].

IrO_2 forms in a rutile structure with space group $P4_2/mnm$ and lattice constants $a = 4.5049$ Å and $c = 3.1587$ Å. Ir atoms form a body-centered tetragonal unit cell. Each Ir atom is coordinated by six oxygens forming a distorted octahedron as shown in Fig. 1(a) consisting of four Ir-O bond lengths of 2 Å and two somewhat shorter bonds of length 1.96 Å. Under the influence of octahedral crystal field, Ir 5*d* bands split into t_{2g} and e_g bands, with t_{2g} contributions lying at a lower energy. The compression of the IrO_6 octahedron shown in the figure by arrows splits the t_{2g} and e_g bands; here, splitting of the t_{2g} bands is shown, which generates a nondegenerate band and a doubly degenerate band. Hybridization of these bands with the O 2*p* levels will form bonding and antibonding orbitals, as schematically shown. The ground-state electronic configuration of Ir^{4+} would be t_{2g}^5. Earlier works proposed a major role of SOC in its electronic structure [17–19]. Considering the

*Corresponding author: kbmaiti@tifr.res.in

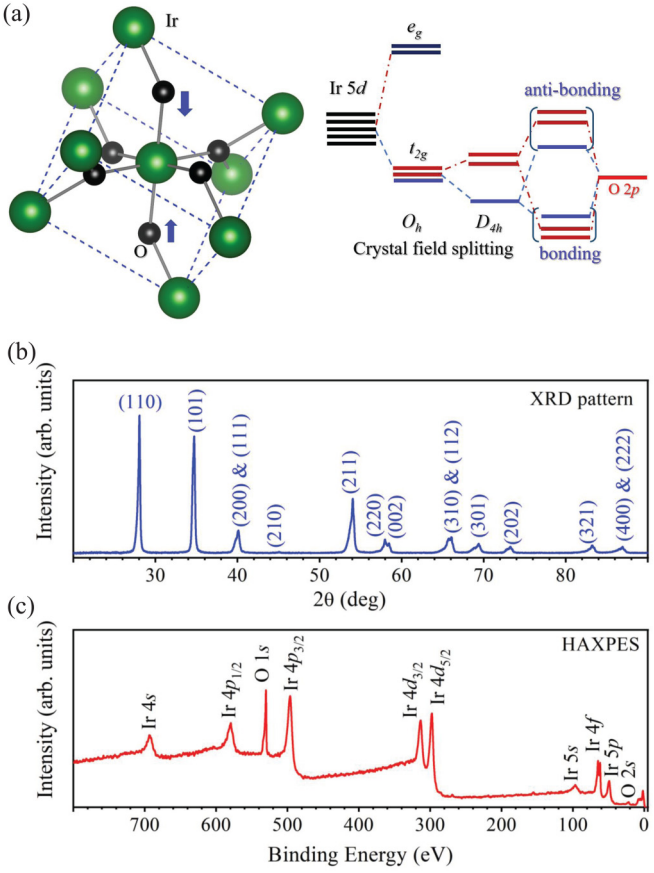

FIG. 1. (a) Crystal structure of IrO_2; the arrows show compression of the Ir-O bond length. The crystal-field splitting of the Ir 5d bands in an octahedral field, O_h and further splitting of t_{2g} bands in D_{4h} symmetry. The splitting of e_g bands in D_{4h} symmetry is not shown. Crystal-field split t_{2g} levels form bonding and antibonding bands due to the hybridization with O 2p states. (b) Powder x-ray diffraction (XRD) pattern of IrO_2 exhibiting a single phase without any impurity peak. (c) Survey scan in the wide energy range collected at room temperature using hard x-ray photon energy.

effective orbital moment, $L_{\text{eff}} = 1$, the degenerate t_{2g} bands spit into two bands with effective total angular momentum, $J_{\text{eff}} = 3/2$ and $1/2$. Thus the bands crossing the Fermi level, ϵ_F, largely possess $J_{\text{eff}} = 1/2$ character and derive the electronic properties of this system. In parallel, another study [20] suggested that crystal-field splitting of the bands due to the distortion of the IrO_6 octahedron lifts the degeneracy of the t_{2g} bands as shown in the figure and hence, the description based on $L_{\text{eff}} = 1$ for the t_{2g} orbitals may not be applicable here. Subsequently, an angle-resolved photoemission study suggested the importance of spin-orbit coupling in the electronic properties [21]. Clearly, the electronic structure of IrO_2 is an outstanding puzzle, and it is important to find out the scenario experimentally on the competing spin-orbit coupling and crystal-field-induced effects in this material.

We report here our results of the investigation of the electronic structure of IrO_2 employing high-resolution photoemission spectroscopy with a variation of surface sensitivity and temperatures. We analyze our results within the framework of the correlated electron systems [1,2,22] and discover signatures of deviation from typical description of the electronic structure for such systems.

II. METHODS

The IrO_2 sample was prepared from commercially available high-quality (purity of 99.9%) IrO_2 powders, which were pelletized using a pressure of 5 tonnes and then sintered at 800 °C for 3 days in air to get a well-sintered hard pellet with large grain size. The structural and elemental characterization of the sample was done by x-ray power diffraction (XRD) and energy-dispersive analysis of x-rays. A typical XRD pattern is shown in Fig. 1(b) exhibiting single phase. We did not find traces of foreign element/phase in our sample.

The photoemission spectroscopy was carried out using a state-of-the-art high-resolution spectrometer equipped with the VG-Scienta R4000 hemispherical electron energy analyzer and monochromatic photon sources. The energy resolution for He I ($h\nu = 21.2$ eV) and He II ($h\nu = 40.8$ eV) spectra was set at 5 meV. For conventional x-ray photoemission spectroscopy (CXPS), we used a monochromatic Al $K\alpha$ ($h\nu = 1486.6$ eV) source; total energy resolution for these measurements was set to 300 meV. In order to enhance the bulk sensitivity of the technique, we carried out hard x-ray photoemission spectroscopy (HXPS) [23] at the synchrotron facility, PETRA III DESY, Hamburg, Germany. The photon energy used was ($h\nu =$) 5947.6 eV and the energy resolution was 150 meV. The sample surfaces for the photoemission measurements were prepared by fracturing the sample via top-post removal method to expose the clean surface. The base pressure of the photoemission spectrometer consisting of laboratory sources was 5×10^{-11} Torr. The pressure in the HXPS spectrometer was 2×10^{-10} Torr during the measurements. The Fermi level was derived from the photoemission spectra of high-quality Ag mounted in electrical contact with the sample. The temperature variation of the sample was achieved by using an open-cycle He cryostat. Since the sample surfaces probed using different setups can be different and the hard x-ray beamline did not have the photon energy below 2.5 keV, we have used the same sample in both sets of experiments, prepared the surface in the ultrahigh vacuum condition, and measurements were done immediately after the surface preparation. The reproducibility of the features was verified after each trial of surface preparations. This ensured that the high-resolution data obtained using laboratory sources and synchrotron sources represent the spectral functions of the same sample.

To characterize the features in the experimental spectra, the electronic band structure calculations were carried out using the full potential linearized augmented plane-wave method within the local spin-density approximations as implemented in WEIN2K software [24]. The lattice parameters reported by Panda *et al.* [18] have been used in the calculations. The exchange-correlation functional used for the calculations was the Perdew-Burke-Ernzerhof functional revised for solids (PBEsol) [25]. The formulation of Anisimov *et al.* [26] was adopted to include the effective Coulomb interaction, U_{eff}, among Ir-5d electrons. We found that the calculated results for various U_{eff} values between 0 and 2 eV provide quite similar descriptions, apart from a small energy shift of the features

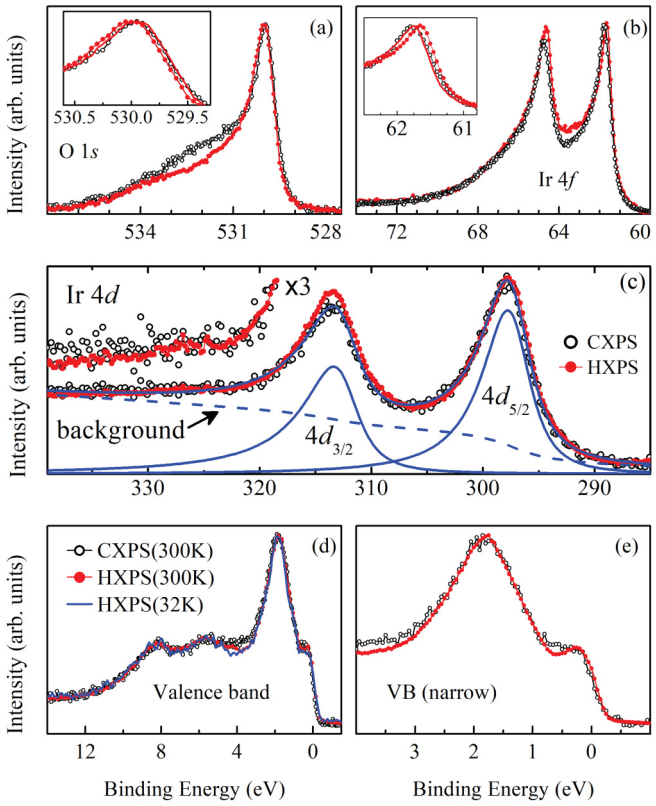

FIG. 2. (a) O 1s, (b) Ir 4f, (c) Ir 4d, (d) valence band (wide), and (e) valence band (close to ϵ_F) spectra collected using conventional XPS (CXPS: open circles) and HXPS (solid circles). Insets in (a) and (b) show the most intense peak in an expanded energy scale. The lines in the insets are the shifted HXPS data providing an energy shift of 100 meV of Ir 4f peak and 50 meV shift of O 1s peak. The lines in (c) are the fit results of Ir 4d CXPS data. The higher-binding-energy region of Ir 4d spectra is shown in an enhanced intensity scale.

consistent with earlier observations [18,19,21]. The results shown here correspond to the calculations including SOC and $U_{\text{eff}} = 2$ eV. The convergence was achieved by considering 1000 k points within the first Brillouin zone.

III. RESULTS AND DISCUSSIONS

To investigate the quality of the sample, a survey scan was collected using HXPS and CXPS. Since HXPS is a highly bulk-sensitive probe (escape depth, λ, of valence electrons is about 40 Å), it represents essentially the bulk electronic structure of the sample. The experimental HXPS survey spectrum collected at room temperature is shown in Fig. 1(c). All the peaks correspond to the excitation of Ir and/or O core and valence electrons, establishing the high purity of the sample.

The surface sensitivity of the photoemission spectroscopy technique becomes most prominent with the smallest escape depth of photoelectrons of about 6 Å for the electron kinetic energy 40–100 eV [27]. Since the electronic structure at the surface can be very different from the bulk electronic structure [28], it is important to verify if such an effect is also present in IrO_2. In Fig. 2 we plot the core-level and valence-band spectra collected using conventional x-ray source of Al $K\alpha$ and hard x-rays from synchrotron. The oxygen 1s spectra shown in Fig. 2(a) exhibit a sharp peak at about 530 eV binding energy along with a feature at 532.4 eV, leading to an asymmetry in the line shape. The intensity at 532.4 eV reduces significantly in the HXPS spectrum due to the increase in bulk sensitivity (λ ∼ 38 Å for HXPS and ∼16 Å for CXPS), manifesting their origin linked to the surface electronic structure. These oxygens could be the surface oxygens, less bound compared to the bulk ones and/or the oxygens adsorbed on the surface. We observe strong asymmetry in the line shape arising from the metallicity of the system. A finite density of states at ϵ_F in metals allows low-energy excitations along with the core-level photoemission that leads to asymmetry in the higher-binding-energy side of the features. Interestingly, the peak position is shifted towards higher binding energies in the HXPS data [see inset of Fig. 2(a)], which is a signature of an enhancement of local potential (Madelung potential) at the oxygen sites in the bulk. The energy shift is estimated to be 50 meV via shifting the HXPS data (line in the inset) and superimposing over the CXPS data.

Ir 4f spectra are shown in Fig. 2(b), exhibiting two sharp peaks at 61.8 eV and 64.8 eV binding energies in the CXPS data (λ ∼ 19.6 Å), indicating a spin-orbit splitting of about 3 eV for the 4f states. In the bulk-sensitive HXPS spectra (λ ∼ 39.9 Å), the peak position is shifted by 100 meV towards lower binding energy; the energy shift is estimated by shifting the HXPS data as shown by a line in the inset of Fig. 2(b). Such an energy shift towards lower binding energy for the cation and the shift of the O 1s peak towards higher binding energy is a signature of an enhancement of covalency (decrease in ionicity) in the bulk electronic structure [29]. Such a scenario may be expected, as the bulk contains complete periodicity of the solid with complete IrO_6 octahedra, while surface often has uncompensated bonds.

In addition, we observe an increase of the $4f_{5/2}$ peak intensity relative to the intensity of the $4f_{7/2}$ peak in the HXPS data. Thus the branching ratio (the ratio of the intensities of Ir $4f_{5/2}$ and Ir $4f_{7/2}$ peaks) is enhanced in the HXPS data, which can happen due to an enhancement of the effective orbital moment in the bulk. The Ir 4d spectra shown in Fig. 2(c) exhibit two intense features at 298 eV and 313.5 eV binding energies corresponding to $4d_{5/2}$ and $4d_{3/2}$ photoemission, respectively. We do not observe discernible features associated to the satellite signal often observed in such core-level spectroscopy due to electron-electron Coulomb repulsion. In order to observe this better, the higher-energy part is shown in an enhanced intensity scale exhibiting a signature of very weak features. All these results demonstrate that the correlation effect, if there is any, will be weak in this system, as expected for 5d orbitals constituting the valence bands having large orbital extensions. Interestingly, the Ir 3d signal also shows enhancement of the $3d_{3/2}$ peak intensity relative to the $3d_{5/2}$ peak in the HXPS spectrum (λ ∼ 39 Å) compared to the CXPS data (λ ∼ 17.9 Å). Spectra collected at different temperatures look very similar to each other.

The total angular momentum, J_c, of the core hole can be expressed as $J_c = L_c \pm S_c$, where L_c and S_c are the orbital and spin quantum numbers of the core hole, respectively. Considering the intensity of the peaks scales with the multiplicity of the eigenstates, the branching ratio for Ir 4f will

be $[2(L_c - S_c) + 1] : [2(L_c + S_c) + 1]$, which is 3:4, and the branching ratio for Ir $4d$ would be 2:3. We have estimated the branching ratio by fitting the core-level spectra using the least-squares error method. We have used the Shirley background function, and the peak shapes were represented by *Pearson IV* functions to capture the asymmetry, experimental resolution broadening, and lifetime broadening. A typical fit is shown by lines in Fig. 2(c) for the case of Ir $4d$ CXPS data. The estimated branching ratio for the $4d$ signal is found to be 0.81 ± 0.05 for CXPS data and 0.85 ± 0.05 for HXPS data, which is significantly higher than the atomic value of 0.67. For the $4f$ signal, this ratio is found to be 0.86 ± 0.05 for the CXPS data and 0.88 ± 0.05 for the HXPS data; the expected value is 0.75. While the atomic description is often found to be good in various core-level spectroscopy results [30], deviation from such a behavior may occur due to the uncompensated electric field at the Ir sites [31]. The spin-orbit coupling strength in an external scalar potential, $V(r)$, can be expressed as $-\frac{e\hbar}{(2mc)^2}\sigma[E(r) \times p]$. Here, $E(r)$ is the electric field [$= -\nabla V(r)$] and p is electron momentum. In IrO_2, $E(r)$ becomes significant, presumably due to the uniaxial anisotropy in the rutile structure as well as local distortions.

In Fig. 2(d) we show the CXPS and HXPS data for the valence band. The near ϵ_F region is shown in Fig. 2(e) in an expanded scale. Both the spectra appear almost identical; a small difference in linewidth is seen due to the energy resolution. Better resolution in the HXPS measurements compared to the CXPS case leads to distinctly defined peaks in the experimental data. This shows that the valence band in the surface and bulk electronic structure are not very different and/or the change in the spectral function is below the sensitivity of the technique. HXPS valence-band data collected at 32 K [blue line in Fig. 2(d)] is superimposed over the room-temperature data (solid red circles) in Fig. 2(d). Spectral features at both the temperatures are found to be almost identical.

The valence-band spectra are investigated in Fig. 3(a), where the data collected using He I, He II, and Al $K\alpha$ photon energies are superimposed over each other after normalization by the intensities near ϵ_F. All the spectra show two distinct features close to ϵ_F with comparable intensities and width. There is a strong monotonic enhancement in intensity beyond about 3 eV binding energy with the decrease in photon energy. The atomic photoemission cross sections [32] of Ir $5d$ states are 24.29, 23.66, and 0.016, and the cross sections of O $2p$ states are 10.67, 5.816 and 0.00023 for photon energies 21.2, 40.8, and 1486.6 eV, respectively. This makes the ratio of the cross sections (O $2p$/Ir $5d$) to be 0.439, 0.246, and 0.014. Clearly, the relative intensity of the O $2p$ signal is the highest in the He I spectrum and becomes insignificant at Al $K\alpha$ photon energy. This suggests that the electronic states constituting the features near ϵ_F possess Ir $5d$ orbital character. The broad features beyond 3 eV are largely comprised of O $2p$ states hybridized with the Ir $5d$ states whose photoemission intensity gets enhanced at He I due to cross-section effects [32], consistent with the description in other transition metal based systems [33].

In order to verify these assertions, we compare the experimental features with the calculated density of states in Fig. 3(b). The Ir $5d$ partial density of states (PDOS) shown by

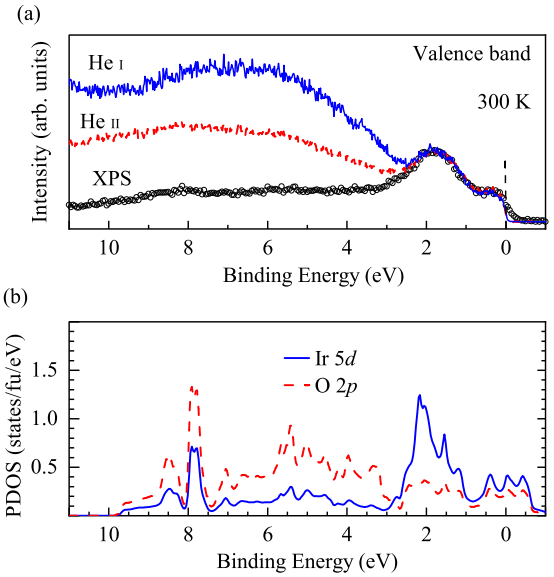

FIG. 3. (a) Valence-band spectra at room temperature collected using photon energies, Al $K\alpha$ (open circles), He II (dashed line), and He I (solid line). (b) The calculated partial density of states of Ir $5d$ (solid line) and O $2p$ (dashed line) states.

the solid line exhibits several features with highest intensity in the vicinity of ϵ_F. Clearly the feature at 2 eV has the highest Ir $5d$ t_{2g} character. The intensities beyond 3 eV are dominated by O $2p$ PDOS contributions. Near 8 eV binding energy, Ir $5d$ PDOS seem to peak, although the dominant contribution is still from O $2p$ PDOS. In fact, we observe Ir $5d$ contributions spanning over the whole energy range due to the presence of π and σ bonding contributions, respectively. All these results reflect the strong covalent nature of the system and are consistent with the experimental observations.

The relative intensities of the two distinct features near ϵ_F remain roughly the same across the photon energies used; a small change could be seen due to the resolution broadening. Note here that the feature near ϵ_F possesses stronger mixed character than the feature at about 2 eV binding energy. Such a difference in the character of the states manifests their independence in properties.

Considering that the features beyond 3 eV represent the contributions from O $2p$ - Ir $5d$ bonding of π and σ type as well as nonbonding O $2p$ intensities, it is tempting to attribute the features near ϵ_F to a $J_{\text{eff}} = 1/2$ and $J_{\text{eff}} = 3/2$ scenario, as often described in the literature [13,18]. It is, however, of note here that the calculations without considering spin-orbit coupling provide a good description of these features. Therefore the necessity to bring in the J_{eff} scenario, which requires strong spin-orbit coupling of degenerate t_{2g} bands, is debatable, although this scenario also provides similar features. Moreover, the distortion of the IrO_6 octahedra lifts the degeneracy of the t_{2g} bands [20].

So far, we have discussed the identification of various features and their association to surface-bulk electronic structures. We now investigate the temperature dependence of the features close to ϵ_F collected with high resolution. In Fig. 4, we show the He I and He II spectra collected at 15 K (solid line) and 300 K (open circles). There are two broad spectral

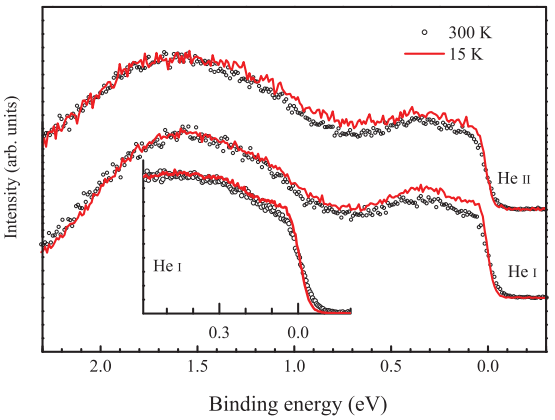

FIG. 4. He I and He II valence-band spectra at 300 K (open circles) and 15 K (solid line). The inset shows the near-ϵ_F part of the He I spectra after normalizing by the intensities at 0.5 eV.

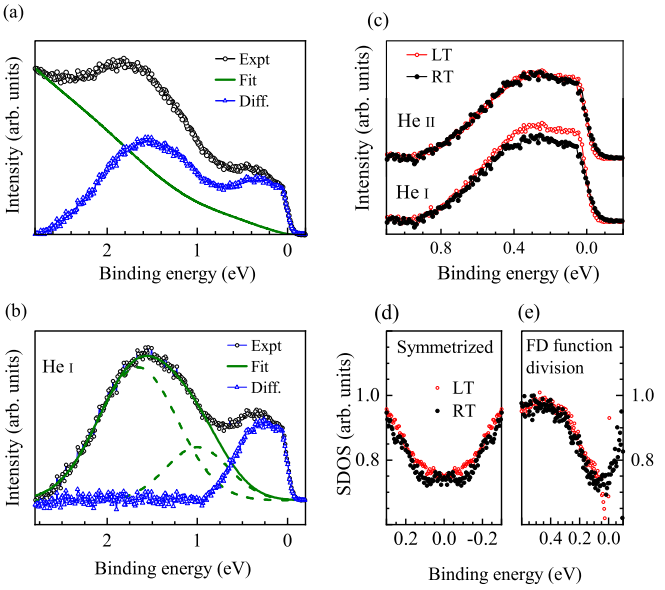

FIG. 5. (a) An example of the subtraction of the tail of higher-binding-energy contributions. Experimental data (open circles), tail (dashed line), and subtracted data (open triangles). (b) An example of the extraction of the near-ϵ_F peaks via subtraction of the higher-energy features (solid line). Dashed lines are the peaks used to derive higher-binding-energy contributions. (c) Near-ϵ_F part from He I and He II spectra collected at 300 K (solid circles) and 15 K (open circles). (d) Spectral density of states (SDOS) calculated via symmetrization of the He I spectra. (e) SDOS extracted by dividing the He I spectra by resolution-broadened Fermi-Dirac function.

regions; one close to ϵ_F and the other beyond 0.7-eV binding energy. The features at higher energies are essentially Ir 5d states having d_{xz}, d_{yz}, and $d_{x^2-y^2}$ symmetry as reported earlier [20]. The intensities near ϵ_F possess d_{xz} and d_{yz} symmetry along with a significant contributions from O 2p states [32]. A normalization of the intensities by the intensity around the 1.5-eV peak exhibits significant enhancement of intensities in the vicinity of ϵ_F at low temperature. While there appears to be an overall increase in intensity in the He II spectra, distinct changes are observed in the He I spectra, exhibiting large enhancement of the near ϵ_F features. Thus, there are two possible conclusions: (i) this enhancement is linked to O 2p contributions and (ii) the states having d_{xz} and d_{yz} have different behavior than the $d_{x^2-y^2}$ states. It is of note here that the apical oxygens (on z axis) are closer to the Ir sites (smaller bond length) compared to those in the xy plane as shown in Fig. 1(a). Therefore d_{xz}/d_{yz} bands will be more covalent due to stronger hybridization. From the experimental results, it appears that the thermal compression enhances the hybridization differently for d_{xz}/d_{yz} and $d_{x^2-y^2}$ orbitals. Such an orbital selective temperature evolution of the spectral functions provides an evidence against the scenario captured considering an $L_{\text{eff}} = 1$ for degenerate t_{2g} bands.

In the inset, we show the region very close to ϵ_F after normalizing by the intensity at 0.5 eV. There is a significant enhancement of the intensity near ϵ_F. In a correlated system, the electron energies are strongly influenced by the electron-electron Coulomb repulsion and the corresponding spectral contributions appear away from ϵ_F—these are called Hubbard bands or incoherent features. In photoemission one probes the lower Hubbard band, while the upper Hubbard band appears in the unoccupied part of the electronic structure. There are contributions from the electrons whose energies are not significantly influenced by the electron correlation effects and appear at ϵ_F—this is called a coherent feature, which can be captured well using density functional theory. With the reduction in temperature, it appears that the intensity of the coherent feature increases at the cost of the incoherent features.

In order to investigate this scenario further, we extracted the Ir 5d contributions via subtracting tail of the higher-binding-energy features, as shown in Fig. 5(a) for the He I room-temperature data. The contributions beyond 1 eV are subtracted as shown in Fig. 5(b)—here, the dashed lines are the peaks used to simulate the intensities beyond 1-eV binding energy. The spectral contributions extracted in this way are shown in Fig. 5(c). We observe an overall enhancement of the intensities in the whole spectral region shown in Fig. 5 in the He I spectra; the He II spectra show marginal change. The larger enhancement in He I spectra indicate the change in intensities is linked to the enhancement of oxygen 2p contributions in this spectral region.

The Fermi-Dirac (FD) distribution function, expressed as $F(\epsilon, T) = 1/[\exp(\frac{\epsilon-\epsilon_F}{k_B T}) + 1]$, changes the spectral intensities in the vicinity of ϵ_F with temperature. Therefore a direct comparison of the raw data at different temperatures near ϵ_F is difficult. The symmetrization of the FD function with respect to ϵ_F ($= 0$ in the binding energy scale) gives unity; $F(\epsilon, T) + F(-\epsilon, T) = 1$. The experimental spectral intensity can be expressed as $I(\epsilon, T) = SDOS(\epsilon, T) \times F(\epsilon, T)$, where "SDOS" represents the spectral density of states. Thus one can extract SDOS by symmetrizing the experimental data as follows: $SDOS(\epsilon, T) = I(\epsilon, T) + I(-\epsilon, T)$ assuming that $SDOS(\epsilon, T)$ is symmetric with respect to ϵ_F. Independent of the properties of SDOS, the extracted intensity at ϵ_F is robust and does not have influence from temperature-dependent FD function. Thus extracted SDOS from the He I data are shown in Fig. 5(d). The results at 300 K and 15 K exhibit almost identical intensity at ϵ_F, with very small enhancement at about 70 meV at 15 K.

It is, however, not *a priori* clear if the spectral function and/or the density of states of IrO_2 is symmetric with respect to ϵ_F. To verify this, we have divided the experimental spectra by the resolution-broadened FD distribution function as follows: $SDOS(\epsilon, T) = I(\epsilon, T)/F(\epsilon, T)$. Since the experimental resolution is good (5 meV), such an estimation provides a good representation of SDOS. The extracted data are shown in Fig. 5(e). The SDOS at both 300 K and 15 K look very similar, with small enhancement just below ϵ_F as seen in Fig. 5(d). The SDOS at 300 K obtained by the FD function division is symmetric with respect to ϵ_F. Clearly, the results in Figs. 5(d) and 5(e) obtained by the two methods provide a consistent scenario. All these results establish that the correlation-induced effect, if there is any, is significantly weak in this system. This is probably the reason for the metallic ground state of this system.

IV. CONCLUSIONS

In summary, we studied the electronic structure of IrO_2 employing high-resolution photoemission spectroscopy. A combination of hard x-ray and conventional x-ray data helped to reveal the surface-bulk differences in the electronic structure. The branching ratio of the Ir core-level spin-orbit split peaks is significantly larger than their atomic values and it enhances in the bulk. This is attributed to an enhancement of the orbital moment due to the uncompensated electric field in solid. Core-level spectra exhibit a signature of enhanced covalency in the bulk compared to the surface. The valence-band spectra exhibit dominant contribution of Ir $5d$ states close to ϵ_F, which is responsible for the electronic properties of this material. The change in surface sensitivity of the technique does not have significant effect in the valence band, and the experimental results could be described well by the effective single-particle description captured within the density functional calculations. Evidently, the electron-correlation-induced effect is not strong in this system, as has also been manifested in the core-level spectroscopy. High-resolution data exhibit multiple features and interesting temperature evolution. The evolution of the spectral features with temperature and photoemission cross sections show orbital selective changes in the valence band, which is an evidence against a purely J_{eff}-based scenario. The covalency of the states close to ϵ_F enhances with the decrease in temperature, and the O $2p$ states play an important role in deriving the electronic properties of this material. These results suggests that while the electron-electron Coulomb repulsion reduces with the enhancement in radial extension in higher-d systems along with an enhancement of spin-orbit coupling, the covalency and the crystal-field effects play important roles with regard to exoticity in these materials.

ACKNOWLEDGMENTS

The authors acknowledge financial support under Project No. 12-R&D-TFR-5.10-0100. K.M. acknowledges financial assistance from DAE-BRNS, Government of India, under the DAE-SRC-OI award program (Grant No. 21/08/2015-BRNS/35034).

[1] A. Georges, G. Kotliar, W. Krauth, and M. J. Rozenberg, Rev. Mod. Phys. **68**, 13 (1996).
[2] M. Imada, A. Fujimori, and Y. Tokura, Rev. Mod. Phys. **70**, 1039 (1998).
[3] G. Cao, S. McCall, M. Shepard, J. E. Crow, and R. P. Guertin, Phys. Rev. B **56**, 321 (1997); P. B. Allen, H. Berger, O. Chauvet, L. Forro, T. Jarlborg, A. Junod, B. Revaz, and G. Santi, *ibid.* **53**, 4393 (1996); J. Okamoto, T. Mizokawa, A. Fujimori, I. Hase, M. Nohara, H. Takagi, Y. Takeda, and M. Takano, *ibid.* **60**, 2281 (1999); C. Martins, M. Aichhorn, and S. Biermann, J. Phys.: Condens. Matter **29**, 263001 (2017).
[4] H. Gretarsson, J. P. Clancy, X. Liu, J. P. Hill, E. Bozin, Y. Singh, S. Manni, P. Gegenwart, J. Kim, A. H. Said *et al.*, Phys. Rev. Lett. **110**, 076402 (2013).
[5] K. Maiti, R. S. Singh, V. R. R. Medicherla, S. Rayaprol, and E. V. Sampathkumaran, Phys. Rev. Lett. **95**, 016404 (2005); K. Maiti, Phys. Rev. B **73**, 115119 (2006).
[6] B. J. Yang and Y. B. Kim, Phys. Rev. B **82**, 085111 (2010).
[7] M. Kargarian, J. Wen, and G. A. Fiete, Phys. Rev. B **83**, 165112 (2011).
[8] R. S. Singh, V. R. R. Medicherla, K. Maiti, and E. V. Sampathkumaran, Phys. Rev. B **77**, 201102(R) (2008); K. Maiti, Solid State Commun. **149**, 1351 (2009).
[9] X. Wan, A. M. Turner, A. Vishwanath, and S. Y. Savrasov, Phys. Rev. B **83**, 205101 (2011).
[10] H. Y. Hwang, Y. Iwasa, M. Kawasaki, B. Keimer, N. Nagaosa, and Y. Tokura, Nat. Mater. **11**, 103 (2015); J. Matsuno, N. Ogawa, K. Yasuda, F. Kagawa, W. Koshibae, N. Nagaosa, Y. Tokura, and M. Kawasaki, Sci. Adv. **2**, e1600304 (2016).
[11] G. K. Wertheim and H. J. Guggenheim, Phys. Rev. B **22**, 4680 (1980).
[12] L. F. Mattheiss, Phys. Rev. B **13**, 2433 (1976).
[13] J. Riga, C. Tenret-Noel, J. J. Pireaux, R. Caudano, J. J. Verbist, and Y. Gobillon, Phys. Scr. **16**, 351 (1977).
[14] M. S. Miao and R. Seshadri, J. Phys.: Condens. Matter **24**, 215503 (2012).
[15] J. P. Clancy, N. Chen, C. Y. Kim, W. F. Chen, K. W. Plumb, B. C. Jeon, T. W. Noh, and Y.-J. Kim, Phys. Rev. B **86**, 195131 (2012).
[16] Y. Hirata, K. Ohgushi, J.-i. Yamaura, H. Ohsumi, S. Takeshita, M. Takata, and T. H. Arima, Phys. Rev. B **87**, 161111(R) (2013).
[17] B. J. Kim, H. Jin, S. J. Moon, J.-Y. Kim, B.-G. Park, C. S. Leem, J. Yu, T. W. Noh, C. Kim, S.-J. Oh *et al.*, Phys. Rev. Lett. **101**, 076402 (2008).
[18] S. K. Panda, S. Bhowal, A. Delin, O. Eriksson, and I. Dasgupta, Phys. Rev. B **89**, 155102 (2014).
[19] Y. Ping, G. Galli, and W. A. Goddard III, J. Phys. Chem. C **119**, 11570 (2015).
[20] J. M. Kahk, C. G. Poll, F. E. Oropeza, J. M. Ablett, D. Céolin, J.-P. Rueff, S. Agrestini, Y. Utsumi, K. D. Tsuei, Y. F. Liao *et al.*, Phys. Rev. Lett. **112**, 117601 (2014).
[21] P. K. Das, J. Sławińska, I. Vobornik, J. Fujii, A. Regoutz, J. M. Kahk, D. O. Scanlon, B. J. Morgan, C. McGuinness,

E. Plekhanov *et al.*, Phys. Rev. Materials **2**, 065001 (2018).

[22] S. Patil, S. K. Pandey, V. R. R. Medicherla, R. S. Singh, R. Bindu, E. V. Sampathkumaran, and K. Maiti, J. Phys.: Condens. Matter **22**, 255602 (2010); S. Patil, V. R. R. Medicherla, R. S. Singh, S. K. Pandey, E. V. Sampathkumaran, and K. Maiti, Phys. Rev. B **82**, 104428 (2010).

[23] C. S. Fadley, in *Hard X-ray Photoelectron Spectroscopy (HAX-PES)*, edited by Joseph C. Woicik, Springer Series in Surface Sciences Vol. 59 (Springer, New York, 2016).

[24] P. Blaha, K. Schwarz, G. K. H. Madsen, D. Kvasnicka, J. Luitz, WIEN2k, An Augmented Plane Wave+Local Orbitals Program for Calculating Crystal Properties (Karlheinz Schwarz, Techn. Universität Wien, Austria).

[25] J. P. Perdew, K. Burke, and M. Ernzerhof, Phys. Rev. Lett. **77**, 3865 (1996).

[26] V. I. Anisimov, I. V. Solovyev, M. A. Korotin, M. T. Czyżyk, and G. A. Sawatzky, Phys. Rev. B **48**, 16929 (1993).

[27] M. P. Seah and W. A. Dench, Surf. Interface Anal. **1**, 2 (1979).

[28] K. Maiti, P. Mahadevan, and D. D. Sarma, Phys. Rev. Lett. **80**, 2885 (1998); K. Maiti, A. Kumar, D. D. Sarma, E. Weschke, and G. Kaindl, Phys. Rev. B **70**, 195112 (2004).

[29] S. J. Kerber, J. J. Bruckner, K. Wozniak, S. Seal, S. Hardcastle, and T. L. Barr, J. Vac. Sci. Technol. A **14**, 1314 (1996).

[30] K. Maiti, P. Mahadevan, and D. D. Sarma, Phys. Rev. B **59**, 12457 (1999); K. Maiti and D. D. Sarma, *ibid.* **58**, 9746 (1998).

[31] A. Pramanik, R. P. Pandeya, K. Ali, B. Joshi, I. Sarkar, P. Moras, P. M. Sheverdyaeva, A. K. Kundu, C. Carbone, A. Thamizhavel *et al.*, Phys. Rev. B **101**, 035426 (2020).

[32] J. J. Yeh and I. Lindau, At. Data Nucl. Data Tables **32**, 1 (1985).

[33] K. Maiti and R. S. Singh, Phys. Rev. B **71**, 161102(R) (2005); K. Maiti, *ibid.* **73**, 235110 (2006); K. Maiti, R. S. Singh, and V. R. R. Medicherla, *ibid.* **76**, 165128 (2007); G. Adhikary, D. Biswas, N. Sahadev, R. Bindu, N. Kumar, S. K. Dhar, A. Thamizhavel, and K. Maiti, J. Appl. Phys. **115**, 123901 (2014).